Physica D 247 (2013) 40–53

Contents lists available at SciVerse ScienceDirect

Physica D

journal homepage: www.elsevier.com/locate/physd

Numerical semi-global analysis of a 1:2 resonant Hopf–Hopf bifurcation

G. Revel *, D.M. Alonso, J.L. Moiola

Instituto de Investigaciones en Ingeniería Eléctrica "Alfredo Desages" (UNS-CONICET), Departamento de Ingeniería Eléctrica y de Computadoras, Universidad Nacional del Sur, B8000CPB Bahía Blanca, Argentina

ARTICLE INFO

Article history:
Received 3 January 2012
Received in revised form
23 November 2012
Accepted 11 December 2012
Available online 20 December 2012
Communicated by H.A. Dijkstra

Keywords:
Hopf–Hopf bifurcation
Strong resonances
Nonlinear oscillators

ABSTRACT

In this paper, a numerical semi-global analysis of the dynamics near a 1:2 resonant Hopf–Hopf bifurcation on a four-dimensional mathematical model of a simple nonlinear oscillator is performed. The 1:2 resonant Hopf–Hopf bifurcation is a codimension-three singularity denoted by two pairs of purely imaginary eigenvalues with frequency ratio 1:2. A structure involving 1:1 and 1:2 resonant Neimark–Sacker bifurcations is clearly identified. Both resonances are coupled by lower-codimension singularities, such as generalized Hopf and period doubling, cusp points, and cyclic fold curves. A three-parameter semi-global analysis is performed and some of the codimension-two singularities unfolded by the 1:2 resonant Hopf–Hopf bifurcation are identified. Several codimension-three points are also detected. The obtained results can be useful for further theoretical analysis of the corresponding normal form.

1. Introduction

The Hopf–Hopf bifurcation can be recognized as a precursor of mode interactions in autonomous nonlinear dynamical systems. Some of these interactions are observed in applications such as those described in [1–6]. The Hopf–Hopf bifurcation is a codimension-two singularity that is characterized by the transversal intersection of two Hopf bifurcation manifolds in the parameter space. Therefore, the corresponding linearization of the system has a pair of critical eigenvalues at $\pm i\omega_1$ and $\pm i\omega_2$, where $\omega_1, \omega_2 > 0$ are called the modes or frequencies, and their ratio plays an important role in the dynamical behavior displayed in a neighborhood of the bifurcation. According to its normal form (see, for example, [7]), when $\omega_1/\omega_2 \neq p/q$ for any pair of positive integers (p, q) such that $p + q \leq 5$, the interaction always gives rise to two-dimensional tori (providing that some other nondegeneracy conditions hold). In some cases (called complex), three-dimensional torus and heteroclinic connections can be added. The scenario associated to the truncated normal form in these cases is well known, and a complete analysis can be found, for example, in [8,7]. When higher-order terms are considered, some of the degeneracies present in the truncated normal form do not persist. In particular, heteroclinic bifurcation curves are destroyed and a more complex structure arises [7]. The full picture in this case is not completely explained in the literature.

More complex and nontrivial mode interactions can arise when the frequencies satisfy $\omega_1/\omega_2 = p/q$ with $p + q \leq 5$. These resonances are observed in applications like delayed systems (see, for example, [9–11]) or mechanical systems [12]. The 1:1 resonance ($p = q = 1$) can generate four codimension-two singularities depending on the unfolding: a generalized Hopf bifurcation (also known as a Bautin bifurcation), a 1:1 resonant Neimark–Sacker bifurcation, a nonresonant Hopf–Hopf bifurcation, and a Fold–Neimark–Sacker bifurcation. This structure is analyzed in [13,14]. The 1:2 resonance was investigated in [15,16], where, among other nontrivial phenomena, evidence of period-doubling bifurcations were reported. The cases p:q with $p = 1$ and $q = 2, 3, 4$ are analyzed in [17], where it is shown that the resonant behavior is transferred to the Neimark–Sacker curves when perturbations of the resonant Hopf–Hopf singularity are considered.

The resonant Hopf–Hopf interaction can lead to complex structures that are detected when a semi-global unfolding is considered. For example, in [18], it is shown numerically that perturbations of the 2:3 resonant Hopf–Hopf interaction can lead to scenarios like those appearing in the study of normal internal resonances in quasiperiodically forced systems [19–21]. In this paper, the dynamical scenario near a 1:2 resonant Hopf–Hopf bifurcation is numerically investigated on a four-dimensional model of a coupled electric oscillator [4]. It is shown that, similarly to the 2:3 resonant case, the scenarios observed in the k:1 and k:2 normal internal resonances are glued together in a nontrivial bifurcation structure. The major challenges involved in a theoretical approach is to describe the emergence, from an equilibrium point, of semi-global structures comprising $R_{1:1}$ and $R_{1:2}$ resonances and their corresponding connection via cyclic fold bifurcations. Thus,

* Corresponding author. Tel.: +54 291 4595180; fax: +54 291 4595154.
E-mail addresses: grevel@uns.edu.ar (G. Revel), dalonso@uns.edu.ar (D.M. Alonso), jmoiola@criba.edu.ar (J.L. Moiola).

0167-2789/$ – see front matter
doi:10.1016/j.physd.2012.12.007

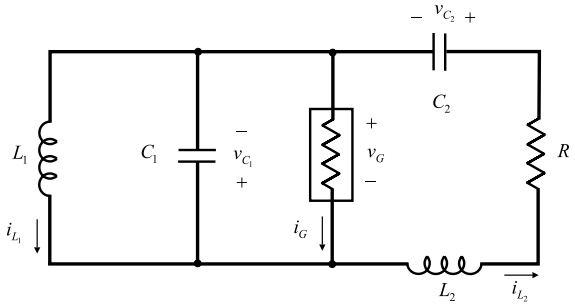

Fig. 1. Schematic representation of the electric oscillator.

our main interest is to reveal numerically new insights in the bifurcation scenario unfolded by the 1:2 resonant Hopf–Hopf singularity that would be useful for further theoretical analysis of the corresponding normal form.

The paper is organized as follows. In Section 2, the mathematical model of the circuit is described. The Hopf–Hopf bifurcations and their resonances are investigated in Section 3. In Section 4, the dynamical scenario near the 1:2 resonant Hopf–Hopf bifurcation is described. The partial three-parameter unfolding of the resonant case is presented in Section 5. In Section 6, other codimension-three degeneracies are described. Finally, in Section 7, some conclusions are included.

2. The electric oscillator

This section describes the circuit of the oscillator used to investigate the dynamics associated to the 1:2 resonant Hopf–Hopf bifurcation. The schematic diagram of the oscillator is shown in Fig. 1. The mathematical model can be easily obtained by applying Kirchhoff's laws, and is given by

$$\begin{aligned}
\dot{x}_1 &= \eta_1 \left(\alpha_1 x_1 + x_2 - x_4 - \alpha_2 x_1^2 - \alpha_3 x_1^3\right),\\
\dot{x}_2 &= -\eta_3 x_1,\\
\dot{x}_3 &= \rho_1 x_4,\\
\dot{x}_4 &= \rho_2 \left(x_1 - x_3 - \eta_2 x_4\right),
\end{aligned} \tag{1}$$

where $x_1 = v_{C_1}, x_2 = i_{L_1}, x_3 = v_{C_2}$, and $x_4 = i_{L_2}$ are the state variables, $v_{C_{1,2}}$ are the voltages (in volts) across the capacitors C_1 and C_2, $i_{L_{1,2}}$ are the currents (in amperes) on the inductances L_1 and L_2, $\eta_1 = 1/C_1$, $\eta_2 = R$, and $\eta_3 = 1/L_1$ are the main bifurcation parameters, $\rho_1 = 1/C_2 = 1 + \sqrt{2}$ and $\rho_2 = 1/L_2 = 2 - \sqrt{2}$ are fixed parameters, and α_1, α_2, and α_3 are auxiliary parameters used to shape the voltage–current characteristic of the nonlinear element according to $i_G = -\alpha_1 v_G - \alpha_2 v_G^2 + \alpha_3 v_G^3$. The resistance R, inductances $L_{1,2}$ and capacitors $C_{1,2}$ are in ohms, henrys and farads, respectively. The values adopted for L_2 and C_2 are such that the values of the angular frequencies ω_1 and ω_2 are between 0.5 and 3 rad/s. In order to obtain practical values for inductances and capacitors, a proper time scaling can be introduced in (1). For example, with the scaling $t = 10^3\tau$, the values of $L_{1,2}$ and $C_{1,2}$ are reduced by a factor of 10^3 (resulting in mHy and μF) and the angular frequency is on the order of 10^3 rad/s.

Similar versions of this circuit were analyzed in [1,22,4]. A remarkable feature of this oscillator is that, by varying a single parameter ($\eta_3 = 1/L_1$), different unfoldings of the Hopf–Hopf bifurcation in the parameter plane (η_1, η_2) are obtained. The interested reader can consult the analysis in [4] for more details. In particular, when variations of three parameters (η_1, η_2, and η_3) are considered, it is possible to find values of these parameters where the ratio between the frequencies of the Hopf bifurcation branches ω_1/ω_2 is p/q, with p and q integers satisfying $p+q \leq 5$, and thus p:q resonant Hopf–Hopf singularities are obtained. These conditions are derived in the next section.

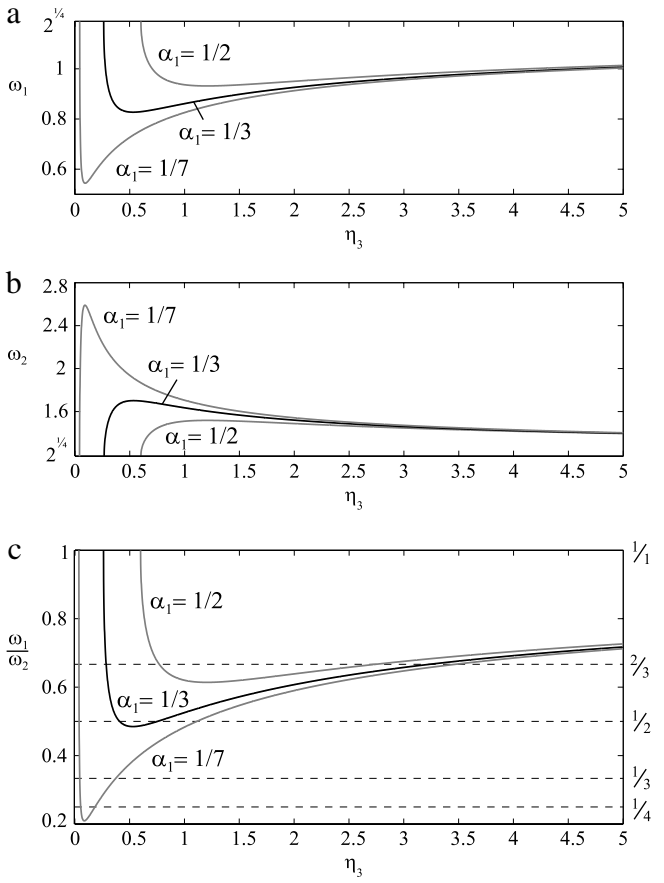

Fig. 2. Frequencies ω_1 and ω_2 and their ratio ω_1/ω_2 on the Hopf–Hopf curve as a function of η_3, for three values of α_1 and with $\rho_1 = 1 + \sqrt{2}$ and $\rho_2 = 2 - \sqrt{2}$.

3. Hopf–Hopf bifurcation analysis

In the main bifurcation parameter space (η_1, η_2, η_3), the mathematical model of the circuit (1) undergoes a Hopf–Hopf bifurcation along the curve defined by

$$HH = \left\{(\eta_1, \eta_2, \eta_3) : \eta_1 = \frac{\rho_1\rho_2}{\eta_3},\ \eta_2 = \frac{\alpha_1\rho_1}{\eta_3},\ \eta_3 \geq \rho_1\alpha_1^2\right\}. \tag{2}$$

On this curve, the system undergoes simultaneously two Hopf bifurcations, namely H_1 and H_2, with frequencies ω_1 and ω_2, respectively. These frequencies can be easily computed, and their values are shown in Fig. 2(a)–(b) as a function of η_3 for three values of α_1 (ρ_1 and ρ_2 are left fixed at $\rho_1 = 1 + \sqrt{2}$ and $\rho_2 = 2 - \sqrt{2}$). In Fig. 2(c), the ratio ω_1/ω_2 at the Hopf–Hopf singularity is shown.

In particular, for $\eta_3 = \rho_1\alpha_1^2$, the frequencies are $\omega_1 = \omega_2 = 2^{1/4}$, and the Hopf–Hopf bifurcation curve HH exhibits a 1:1 resonance at

$$HH_{1:1} = (\eta_1, \eta_2, \eta_3) = \left(\frac{\rho_2}{\alpha_1^2}, \frac{1}{\alpha_1}, \rho_1\alpha_1^2\right). \tag{3}$$

The normal form of this bifurcation was studied in [13,14]. According to its coefficients, it can generate four codimension-two singularities: a generalized Hopf bifurcation, a 1:1 resonant Neimark–Sacker bifurcation, a nonresonant Hopf–Hopf bifurcation, and a Fold–Neimark–Sacker bifurcation.

For increasing values of parameter η_3, the curve HH can exhibit additional resonances depending on the value of the auxiliary parameter α_1. This feature is illustrated in Fig. 2(c), where the horizontal dashed lines denote frequency relations p/q, with integers (p, q) such that $p + q \leq 5$, leading to resonance conditions. Notice

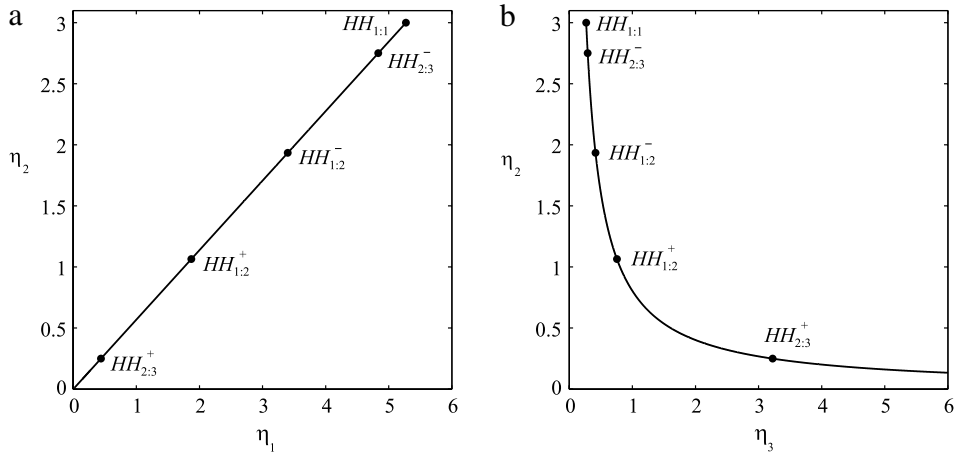

Fig. 3. Hopf–Hopf bifurcation curve varying η_1, η_2, and η_3, for $\alpha_1 = 1/3$, $\rho_1 = 1+\sqrt{2}$ and $\rho_2 = 2-\sqrt{2}$. (a) Projection over the plane (η_1, η_2). (b) Projection on the plane (η_3, η_2).

that for $\alpha_1 = 1/7$ the five cases can be reproduced. Specifically, when $0 < \alpha_1 < \sqrt{\frac{3}{2}\frac{\rho_2}{\rho_1}} \simeq 0.6033$, the curve HH undergoes a pair of 2:3 resonances at

$$HH_{2:3}^{\pm} = (\eta_1, \eta_2, \eta_3) = \left(\frac{\rho_1}{3\delta_1^{\pm}}, \frac{\alpha_1\rho_1}{3\rho_2\delta_1^{\pm}}, 3\rho_2\delta_1^{\pm}\right), \tag{4}$$

with $\delta_1^{\pm} = \left(1 \pm \sqrt{1 - \frac{2}{3}\alpha_1^2\frac{\rho_1}{\rho_2}}\right)$. Both points coalesce for $\alpha_1 = \sqrt{\frac{3}{2}\frac{\rho_2}{\rho_1}} \simeq 0.6033$. A numerical analysis of the unfolding of the 2:3 resonance can be consulted in [18], where it is shown that the singularity generates a period-doubling bubble with two 1:2 strong resonances on one of the Neimark–Sacker branches of the Hopf–Hopf bifurcation, and a 1:3 strong resonance on the other branch. The semi-global bifurcation structure is completed by a curve of saddle–node bifurcations of limit cycles that connects both resonance scenarios.

If $0 < \alpha_1 < \sqrt{\frac{1}{2}\frac{\rho_2}{\rho_1}} \simeq 0.3483$, the system also undergoes a pair of 1:2 resonances ($HH_{1:2}$) at the points

$$HH_{1:2}^{\pm} = (\eta_1, \eta_2, \eta_3) = \left(\frac{\rho_1}{\delta_2^{\pm}}, \frac{\alpha_1\rho_1}{\rho_2\delta_2^{\pm}}, \rho_2\delta_2^{\pm}\right), \tag{5}$$

with $\delta_2^{\pm} = \left(1 \pm \sqrt{1 - 2\alpha_1^2\frac{\rho_1}{\rho_2}}\right)$. This type of resonance was studied in [15,16], where, among other nontrivial phenomena, evidence of period-doubling bifurcations was reported. Analogously, by decreasing the value of α_1, 1:3 and 1:4 resonances can be created.

Since we are interested in studying the semi-global unfolding of the 1:2 Hopf–Hopf bifurcation, the parameter α_1 is settled at $\alpha_1 = 1/3$. For this value of the auxiliary parameter, 1:1, 1:2, and 2:3 resonances can be detected (see Fig. 2(c)), and the projections of the Hopf–Hopf curve HH over the parameter planes (η_1, η_2) and (η_3, η_2) are shown in Fig. 3(a)–(b), respectively. In order to identify some nonlocal bifurcation structures organized by the 1:2 Hopf–Hopf resonance, a numerical study around the point $HH_{1:2}^{-}$, located at $(\eta_1, \eta_2, \eta_3) \approx (3.4007222, 1.9351329, 0.4158568)$, is performed. Similar results are expected to occur in the neighborhood of $HH_{1:2}^{+}$.

4. Dynamical scenario for parameter values close to the 1:2 Hopf–Hopf bifurcation condition

Let us begin the analysis of the dynamical scenario associated to the 1:2 resonant Hopf–Hopf bifurcation by computing the bifurcation diagram on the parameter plane (η_1, η_2) for $\eta_3 = 0.41$, i.e. close to the resonance point $HH_{1:2}^{-}$ (detected at $\eta_3 = 0.4158568$). For simplicity, this point is denoted as $HH_{1:2}$ in the following. The other parameters are left fixed at $\alpha_1 = 1/3$, $\alpha_2 = 0.01$, $\alpha_3 = 1$, $\rho_1 = 1+\sqrt{2}$ and $\rho_2 = 2-\sqrt{2}$. All the continuations were performed with MATCONT [23].

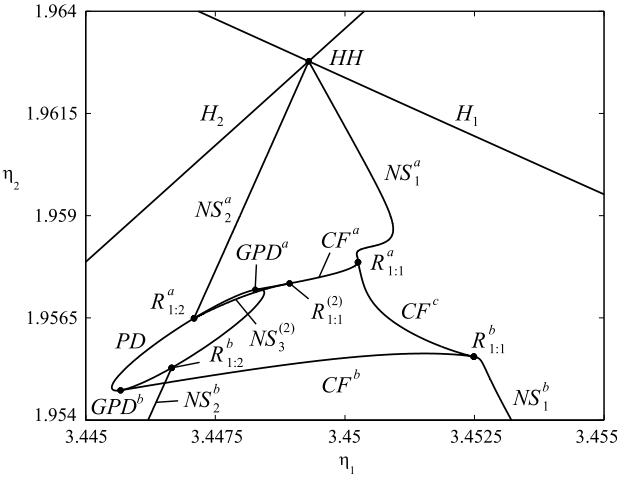

Fig. 4. Bifurcation diagram for $\eta_3 = 0.41$.

The bifurcation diagram for $\eta_3 = 0.41$ is shown in Fig. 4. For simplicity, the acronyms used in this and the following diagrams are summarized in Tables 1 and 2. Computing the coefficients of the normal form of the Hopf–Hopf bifurcation with MATCONT results in $p_{11} \cdot p_{22} > 0$, $\theta = 3.985044$, $\delta = 1.003584$, $\theta\delta > 1$, according to the notation in [7]. The unfolding corresponds to one of the simple cases of the 11 unfoldings of the nonresonant Hopf–Hopf bifurcation, and the phase portraits can be consulted in that book (called Case I) or in [8]. The normal form for this case predicts (locally) the existence of two Neimark–Sacker bifurcation curves NS_1^a and NS_2^a related to the Hopf branches H_1 and H_2, respectively (see Fig. 4).

From Fig. 4, it is clear that, when considering a larger region of the parameter plane, two different bifurcation structures on the Neimark–Sacker curves can be clearly identified. The first one arises on the branch NS_1 (on the right), and it is composed basically by two Neimark–Sacker bifurcation curves $NS_1^{a,b}$, two strong 1:1 resonances $R_{1:1}^{a,b}$, two cusp points $C^{a,b}$ (not shown), and three cyclic fold curves $CF^{a,b,c}$. The second structure is on the branch NS_2 (on the left), and it involves two Neimark–Sacker bifurcation curves

Table 1
List of detected bifurcations of equilibria and the acronyms used in the paper. The coefficients l_1 and l_2 are, respectively, the first and second Lyapunov coefficients of the Hopf bifurcation normal form.

Label	Bifurcation	Eigenvalues	Degeneracy	Codim.
H	Hopf	$\lambda_{1,2} = \pm i\omega$	–	1
H_{10}	Generalized Hopf (Bautin)	$\lambda_{1,2} = \pm i\omega$	$l_1 = 0$	2
HH	Hopf–Hopf	$\lambda_{1,2} = \pm i\omega_1$, $\lambda_{3,4} = \pm i\omega_2$	–	2
H_{20}	Doubly degenerate Hopf	$\lambda_{1,2} = \pm i\omega$	$l_1 = l_2 = 0$	3
$HH_{p:q}$	p:q resonant Hopf–Hopf	$\lambda_{1,2} = \pm i\omega_1$, $\lambda_{3,4} = \pm i\omega_2$ with $\omega_1/\omega_2 = p/q$	–	3

Table 2
List of detected limit cycle bifurcations and the acronyms used in the paper. Notes: (a) the coefficient of the first nonlinear term of the corresponding normal form is zero; (b) the first and second nonlinear terms of the cusp normal form are zero; (c) as (b), for the period-doubling normal form; (d) the first nonlinear term of the period-doubling normal form involved is zero.

Label	Bifurcation	Multipliers	Degeneracy	Codim.
CF	Cyclic fold	$\mu_1 = 1$	–	1
PD	Period doubling or flip	$\mu_1 = -1$	–	1
NS	Neimark–Sacker	$\mu_{1,2} = e^{\pm i\theta}$	–	1
C	Cusp	$\mu_1 = 1$	Note (a)	2
GPD	Generalized period doubling	$\mu_1 = -1$	Note (a)	2
CH	Generalized NS (Chenciner)	$\mu_{1,2} = e^{\pm i\theta}$	Note (a)	2
$R_{1:1}$	1:1 strong resonance	$\mu_{1,2} = 1$	–	2
$R_{1:2}$	1:2 strong resonance	$\mu_{1,2} = -1$	–	2
FNS	Fold–Neimark–Sacker	$\mu_1 = 1$, $\mu_{2,3} = e^{\pm i\theta}$	–	2
ST	Swallowtail	$\mu_1 = 1$	Note (b)	3
DPD	Doubly degenerate PD	$\mu_1 = -1$	Note (c)	3
B	$R_{1:2}$–GPD interaction	$\mu_{1,2} = -1$	Note (d)	3
A	FNS–$R_{1:1}$ interaction	$\mu_{1,2,3} = 1$	–	3

$NS_2^{a,b}$, two strong 1:2 resonances $R_{1:2}^{a,b}$, a period-doubling bubble PD, two generalized period-doubling bifurcation points $GPD^{a,b}$, and two cyclic fold curves $CF^{a,b}$. These structures can be associated to those observed separately in the study of normal internal k:1 and k:2 resonances in quasiperiodically forced oscillators [19–21,24]. In this case, both structures are connected each other by the cyclic fold curves CF^a and CF^b, leading to a new structure.

4.1. Semi-structure associated to the branch NS_1

The local codimension-one and codimension-two bifurcations of limit cycles involved in the structure associated to the branch NS_1 of Fig. 4 are shown in detail in Fig. 5. All of the local bifurcations predicted by the normal form of k:1 normal internal resonance are found here. Some additional bifurcations are also detected. Nonlocal bifurcations such as homoclinic and saddle–node bifurcations of the torus, observed in the normal form, are not studied here. The reader is referred to [24] for details on these and other global bifurcations.

The interactions between the three cyclic fold curves $CF^{a,b,c}$ and the Neimark–Sacker curves $NS_1^{a,b}$ are shown in the magnified rectangles of Fig. 5. The upper one (reproduced schematically in Fig. 6(a) for the sake of clarity) shows the bifurcation diagram in the neighborhood of $R_{1:1}^a$, and the lower one (reproduced in Fig. 6(b)) depicts the scenario for $R_{1:1}^b$. The descriptions of the labels are listed in Table 2.

There are some differences between the semi-global structure of Fig. 5 and the one observed in [24] for the k:1 normal internal resonance. One of them is the presence of two (rather than one) Chenciner bifurcations (CH) near to $R_{1:1}^a$. The second one is the existence of a Fold–Neimark–Sacker bifurcation [25,26] and a Chenciner singularity near to $R_{1:1}^b$ on the curve NS_1^b that is associated to the limit cycle born at the Hopf bifurcation H_1 (see

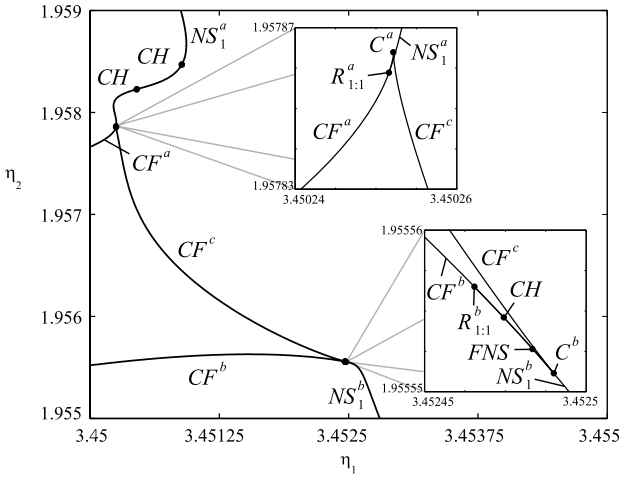

Fig. 5. Bifurcation structure associated to the 1:1 resonances ($\eta_3 = 0.41$).

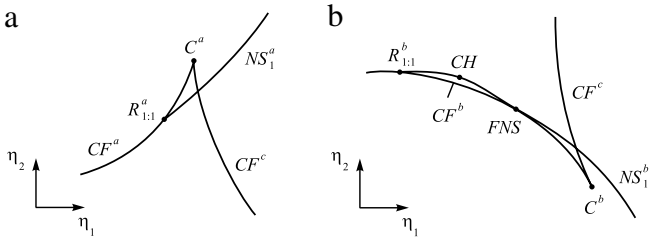

Fig. 6. Schematic view in a vicinity of (a) $R_{1:1}^a$ (upper rectangle of Fig. 5); (b) $R_{1:1}^b$ (lower rectangle of Fig. 5).

Fig. 6(b)). Although the Fold–Neimark–Sacker (FNS) bifurcation is not directly connected to the 1:2 resonant Hopf–Hopf bifurcation, it will be shown that it interacts with $R_{1:1}^b$ in a codimension-three bifurcation with three nontrivial multipliers equal to one.

4.2. Semi-structure associated to the branch NS_2

The bifurcation diagram in a vicinity of the period-doubling bubble on the branch NS_2 is shown in Fig. 7. Again only local codimension-one and codimension-two bifurcations of limit cycles are depicted. The semi-global bifurcation scenario is the same that those observed numerically in [27,18] and theoretically in [19–21,24]. The main feature of this structure is the existence of two 1:2 strong resonances, namely $R_{1:2}^a$ and $R_{1:2}^b$, connected by a period-doubling bubble PD. The Neimark–Sacker curve NS_2^a, arising from the Hopf–Hopf bifurcation, ends at the resonance point $R_{1:2}^a$. This point also unfolds a Neimark–Sacker bifurcation of the period-two cycle $NS_3^{(2)}$ that ends at the 1:1 resonance $R_{1:1}^{(2)}$ (the superscript 2 indicates that it corresponds to a period-two cycle) on the cyclic fold curve CF^a. On the opposite side of the bubble, a new Neimark–Sacker curve NS_2^b arises at the resonance point $R_{1:2}^b$. In the vicinity of this point, a Chenciner bifurcation CH exists. The period-doubling bubble suffers two generalized period-doubling bifurcations GPD^a and GPD^b where the cyclic fold curves CF^a and CF^b arise. These curves interact on the right with the resonant scenario on the branch NS_1. The local dynamics, including the global bifurcations, associated with the resonances $R_{1:2}^a$ and $R_{1:2}^b$ can be observed in [24].

4.3. Dynamical behaviors associated to the semi-global bifurcation structure

The dynamical behavior arising in the semi-global structure depicted in Fig. 4 can be further interpreted with the aid of one-parameter bifurcation diagrams. Towards this end, continuations

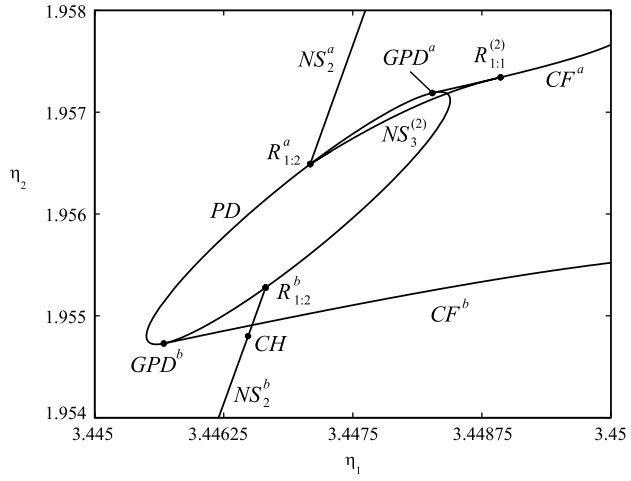

Fig. 7. Expanded view of the period-doubling isle and the related bifurcations for $\eta_3 = 0.41$.

varying η_1 for different (fixed) values of η_2 with $\eta_3 = 0.41$ were performed. The diagrams, corresponding to horizontal segments in Fig. 4, are shown in Fig. 8. The characteristic multipliers of the cycles at the bifurcation points are also shown. The arrows denote the crossing direction of the critical multipliers when parameter η_1 is varied according to the arrows in the continuation locus. The equilibrium point at the origin is unstable and is denoted as a dashed line; stable limit cycles are denoted by filled circles and unstable ones by empty circles.

The main effect of the structure is on the limit cycles born at the Hopf bifurcations H_1 and H_2. The simplest dynamical scenario corresponds to the cases depicted in Fig. 8(a) for $\eta_2 = 1.959$ (i.e. above the bifurcation structure) and in Fig. 8(i) for $\eta_2 = 1.954$ (below the structure). The situation in these cases is qualitatively the same: two unstable limit cycles arise at H_1 and H_2, and then they become stable at the Neimark–Sacker bifurcations NS_1 and NS_2, respectively. At these bifurcation points a pair of complex multipliers crosses the unit circle near $+1$ for the cycle born at H_1, and near -1 for that associated to H_2. For η_1 between NS_1 and NS_2, both qualitatively different stable limit cycles coexist with an unstable two-dimensional (2D) torus (not shown in the figures). These coexisting cycles can be seen in Fig. 9, where their projections on the plane $x_1 - x_2$ and the time signals in the stationary regime for $\eta_1 = 3.449$ are shown. The limit cycle lc_1 with period $T = 7.4670$ s($\omega = 0.8415$ rad/s) is the one born at H_1, and the cycle lc_2 with $T = 3.7394$ s ($\omega = 1.6803$ rad/s) arises at H_2. Notice that the frequency relation is approximately 1:2. The 2D torus arisen in the Neimark–Sacker bifurcations is unstable and restricts the basin of attraction. For values of η_1 greater than that corresponding to NS_1, only one stable limit cycle exists, namely lc_2. Similarly, for η_1 lower than the value of NS_2, the only stable limit cycle is lc_1.

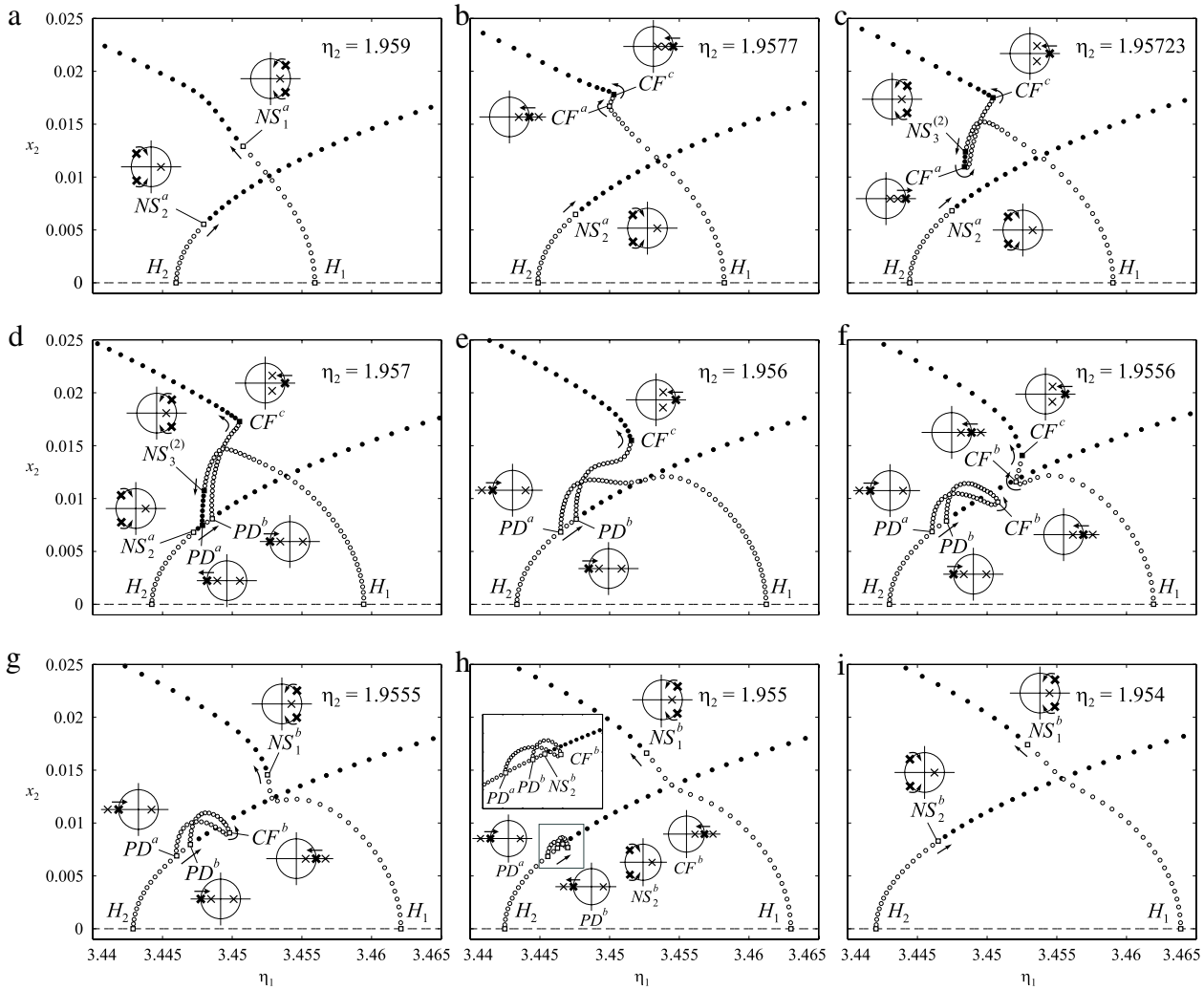

Fig. 8. One-parameter bifurcation diagrams for different values of η_2 ($\eta_3 = 0.41$).

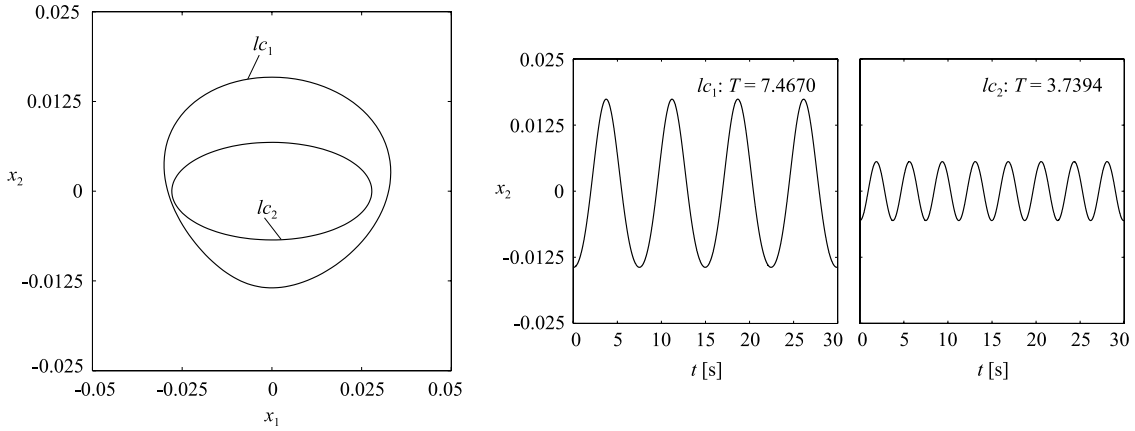

Fig. 9. Dynamical behavior in the stationary regime for $\eta_1 = 3.449$ and $\eta_2 = 1.959$.

For intermediate values of η_2, the structure introduces other bifurcation phenomena leading to additional periodic and quasiperiodic orbits (Fig. 8(b)–(h)). The global structure of cycles is very complex due to the presence of homoclinic and heteroclinic bifurcations. Therefore, in Fig. 8, only the local bifurcations of limit cycles are depicted. Most of the additional limit cycles and quasiperiodic orbits are unstable, and they affect the transient behaviors and the basins of attraction of the stable cycles. Nevertheless, in some of the cases, additional stable limit cycles coexist with the original ones (lc_1 and lc_2). For example, let us analyze in detail the situation of Fig. 8(d) for $\eta_2 = 1.957$.

In order to describe the dynamical scenario, the Poincaré section $x_1 = 0, \dot{x}_1 > 0$ is chosen, and projections of the iterates on the x_2–x_3 plane are evaluated for different key values of η_1. The results are shown in Fig. 10, where the most relevant part of the continuation diagram is magnified in the center. The main features will be described below, but it is clear that, in this case, the cycle lc_2 undergoes period-doubling bifurcations caused by the *PD* bubble in Fig. 4. On the other hand, the cycle lc_1, is now disconnected from H_1 (transition from Fig. 8(c) to Fig. 8(d)), but it retains the shape and period of that born at H_1. Let us begin the description of Fig. 10 at $\eta_1 = 3.447$, where the cycle lc_1 is stable and lc_2 is unstable (of saddle-focus type). The corresponding iterations are shown in Fig. 10(a), where the stable cycle lc_1 (stable fixed point) is denoted with a filled circle and the unstable one lc_2 with an empty circle. For increasing values of η_1, the cycle lc_2 undergoes a Neimark–Sacker bifurcation NS_2^a, it becomes stable, and an unstable 2D torus arises, namely tr_2. The continuation of tr_2 is not shown in the diagram, but it evolves towards the right. The situation for $\eta_1 = 3.4475$ is shown in map (b). The cycle lc_2 loses its stability (to a saddle type) due to PD^a, and a period-two stable cycle lc_3 emerges. The situation for $\eta_1 = 3.4479$ is depicted in map (c). For a better interpretation of the cycles the corresponding phase portrait and time series are shown in Fig. 11. The period-two stable cycle lc_3 coexists with lc_1 (stable) and lc_2 (unstable). Notice that the cycle lc_3 practically has the same period of lc_1, but with very different amplitudes and waveforms.

Then, the period-two cycle lc_3 undergoes a Neimark–Sacker bifurcation $NS_3^{(2)}$ leading to a stable 2D torus, namely tr_3. The torus evolves to the right, and the scenario for $\eta_1 = 3.44803$ is depicted in map (d). Very close to $NS_3^{(2)}$, the torus exhibits a homoclinic bifurcation (forming the typical "eight figure"), and thus, a "big" torus is formed as depicted in map (e) for $\eta_1 = 3.44805$. To illustrate the emerging dynamical behavior, the corresponding phase portrait and time series are shown in Fig. 12. Comparing to Fig. 11, the cycles lc_1 and lc_2 remain practically unchanged, but now lc_3 is unstable with a slight change in its waveform, and the stable torus tr_3 competes with lc_1. Remember that an unstable torus tr_2 (not shown in this figure) coexists with these invariant sets. The time evolution of the torus was obtained with the initial condition $(x_1, x_2, x_3, x_4) = (0.0001, 0, 0, 0)$, and after an abrupt change in amplitude the oscillation reaches tr_3. Three different waveforms are depicted in Fig. 12(a)–(c) for $t \in (100\,000, 100\,030)$, $t \in (110\,000, 110\,030)$, and $t \in (120\,000, 120\,030)$, respectively. In order to facilitate the comparison with the previously shown waveforms, the origin of the time axis is set at $t = 0$. Since the new frequency introduced by the Neimark–Sacker bifurcation is very low compared to that of the period-two cycle, if only a few cycles are observed, the behavior could be interpreted as a period-two cycle instead of a torus. This fact is confirmed by computing the rotation number on the second iterated map, i.e. considering impacts once every two iterates on the Poincaré section. The rotation number is approximately 1.03×10^{-4}, revealing that the torus is close to a period-two cycle as is expected in a 1:2 strong resonance.

The period-two stable torus tr_3 survives for a narrow band of the parameter space until it collapses with tr_2 in a saddle–node bifurcation. The resulting scenario is shown in map (f) for $\eta_1 = 3.4481$. Notice that all of these interactions are in accordance to the dynamics predicted by the normal form of the Neimark–Sacker 1:2 strong resonance. Between $\eta_1 = 3.4481$ (map (f)) and $\eta_1 = 3.44814$ (map (g)), a global change in the connections among cycles occurs. Although this is not a bifurcation, it paves the way for the following interactions with the period-one cycle lc_1. For increasing values of η_1, the cycle lc_2 becomes stable after the period-doubling bifurcation PD^b, and a second period-two unstable cycle lc_4 arises. This situation is depicted in map (h) for $\eta_1 = 3.4485$. The corresponding phase portraits and time series for this case are shown in Fig. 13.

The period-two cycles lc_3 and lc_4 evolve, and they begin to impact only one time on the Poincaré section. This case is depicted in map (i) for $\eta_1 = 3.4503$, i.e. close to the cyclic fold bifurcation CF^c. Remember that this bifurcation is related to the substructure associated to the Neimark–Sacker 1:1 strong resonance. The phase portraits and time series are shown in Fig. 14, where the qualitative changes in the waveforms of the former period-two cycles lc_3 and lc_4 are evident. At CF^c, the cycles lc_1 and lc_4 collide, and for increasing values of η_1 only two cycles exist, lc_2 (stable) and lc_3 (unstable), as depicted in map (j) for $\eta_1 = 3.451$.

In order to investigate the dynamics on the whole domain of Fig. 4, and for completing the information given by the local bifurcation diagrams, the Poincaré sections, and the time series in Figs. 8–14, a computation of the Lyapunov exponents was carried out. Towards this end, the parameter domain (η_1, η_2) in Fig. 4 was divided into a grid of 500 × 500 equally spaced

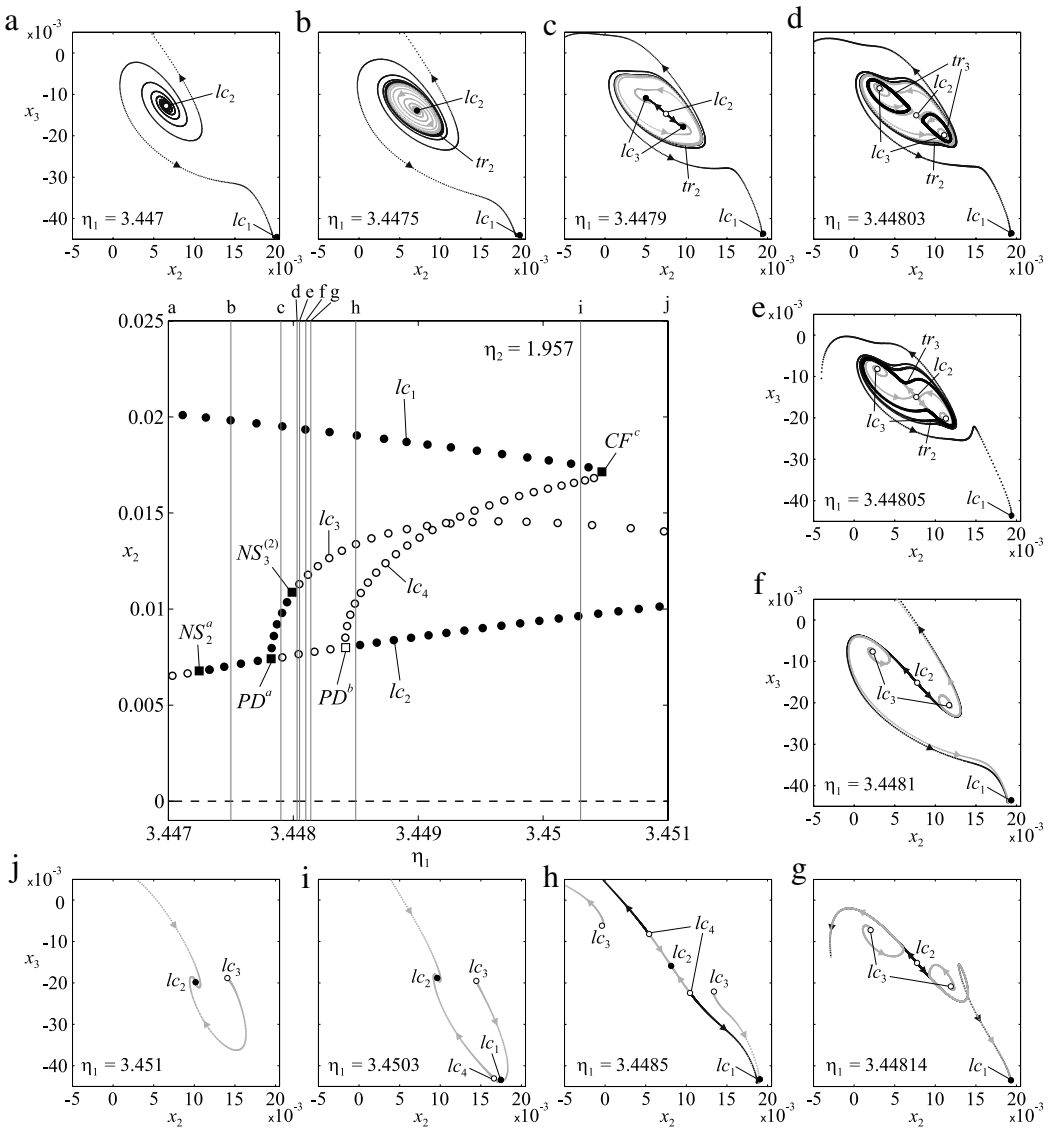

Fig. 10. Projections of the Poincaré iterates for different values of η_1 with $\eta_2 = 1.959$.

points, and simulations with the initial condition $(x_1, x_2, x_3, x_4) = (0.0001, 0, 0, 0)$ were performed. The first 30×10^4 s were discarded and the following 20×10^4 s were used to compute the Lyapunov exponents. The results are displayed in Fig. 15 (left), where the value of the closest to zero Lyapunov exponent is shown (brighter points means closest to zero values). Notice that, when the largest Lyapunov exponent was found to be zero, the value of the following nonzero exponent was used. For a better interpretation of the results, the bifurcation diagram of Fig. 4 is superimposed. In Fig. 15 (left), three regions are clearly identified. The green one, where all the exponents are negative, corresponds to the stable equilibrium point at the origin, and the gray ones correspond to periodic orbits (one of the exponents is zero): in the left region (darker) the attracting set is lc_1, and in the right one (brighter) it is lc_2.

To increase the detail in the region where the period-doubling orbits lc_3 and 2D torus tr_3 exist, a new grid of 200×120 equally spaced points on the region depicted by the rectangle was performed. Since the transient behavior near the bifurcation curves is extremely large, to ensure that the trajectories converge to the true solution, the first 150×10^4 s of the simulations were discarded and the following 50×10^4 s were used to compute the Lyapunov exponents. The results are shown in the right, where the period-doubling orbit lc_3 and the torus tr_3 are indicated. The latter is depicted in cyan since a second Lyapunov exponent is zero. Thus, only the attracting sets described in Figs. 8–14, i.e. the limit cycles lc_1, lc_2, lc_3 and the 2D torus tr_3, were detected. The cycles lc_1 and lc_2 constitute the most common behavior to be observed in this region of parameters, while the attracting sets lc_3 and tr_3 are confined to a very small region near to the curves *PD* (in the segment between $R^a_{1:2}$ and GPD^a) and $NS_3^{(2)}$, respectively. No evidence of other stable cycles or attractors was observed.

5. The 1:2 Hopf–Hopf bifurcation as an organizing centre of the dynamics

In order to investigate the origin of the ensemble depicted in Fig. 4 and its connection with the $HH_{1:2}$ resonance, a three-parameter continuation of the codimension-two bifurcation points shown in that figure (and those in the expanded views of Figs. 5–7) is performed. This continuation is carried out manually, i.e. by means of two-parameter slices (on the plane η_1–η_2) for increasing values of η_3. The first slice is the one shown in Fig. 4 for $\eta_3 = 0.41$.

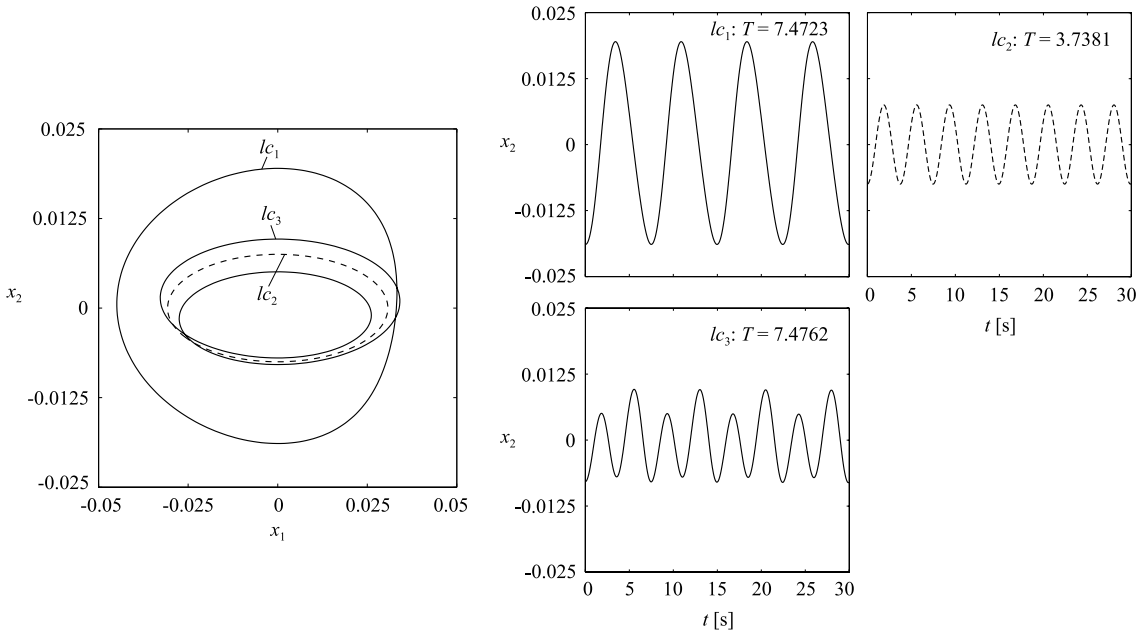

Fig. 11. Dynamical behavior in the stationary regime for $\eta_1 = 3.4479$ and $\eta_2 = 1.957$ (map (c) in Fig. 10).

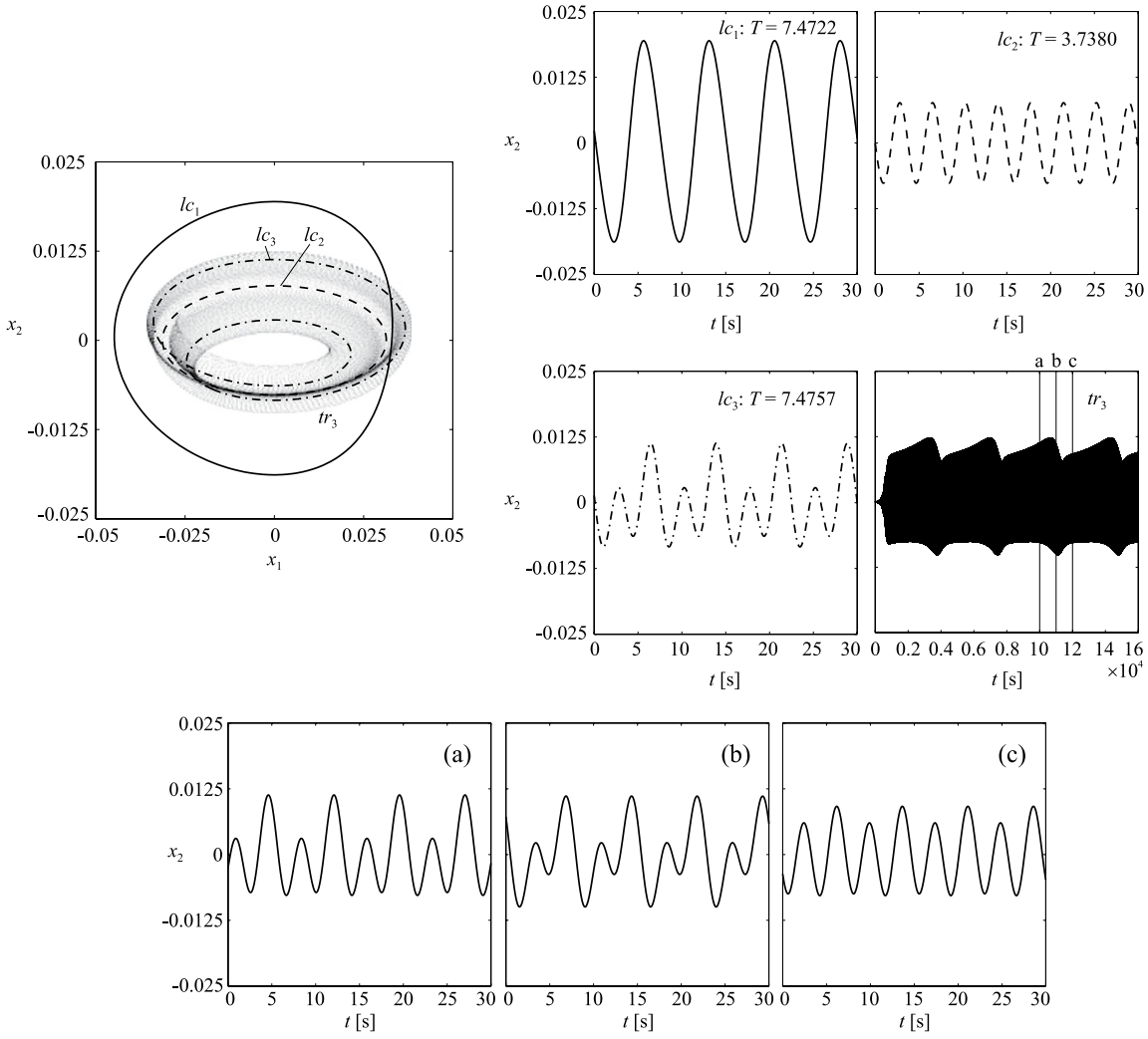

Fig. 12. Dynamical behavior for $\eta_1 = 3.44805$ and $\eta_2 = 1.957$ (map (e) in Fig. 10).

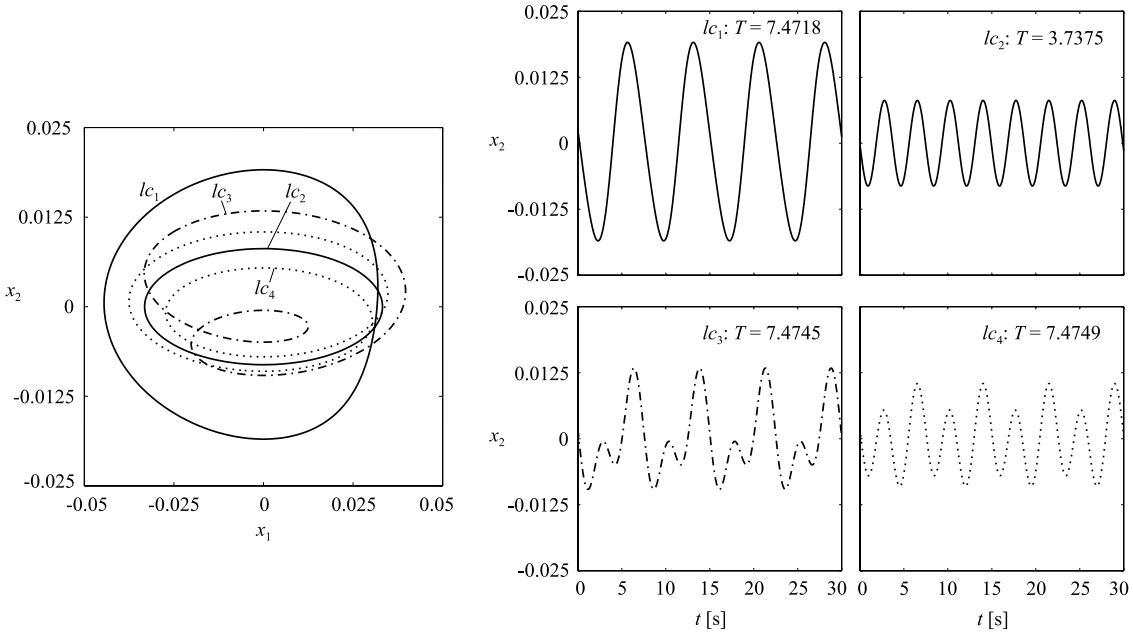

Fig. 13. Dynamical behavior in the stationary regime for $\eta_1 = 3.4485$ and $\eta_2 = 1.957$ (map (h) in Fig. 10).

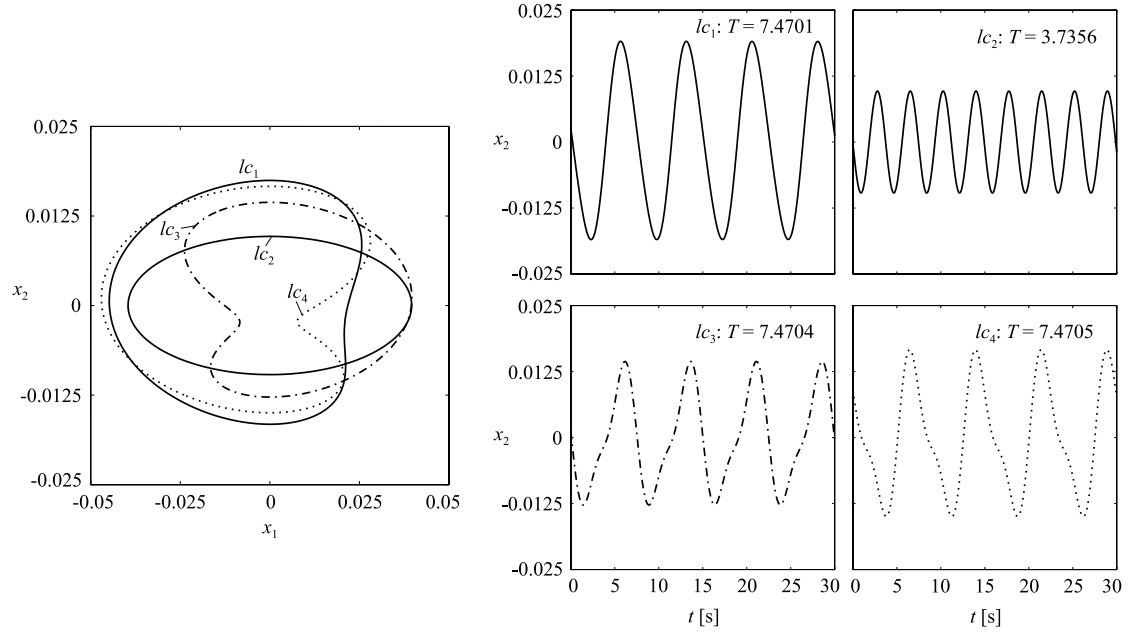

Fig. 14. Dynamical behavior in the stationary regime for $\eta_1 = 3.4503$ and $\eta_2 = 1.957$ (map (i) in Fig. 10).

Then the value of η_3 is increased with a sufficiently small step size and the corresponding bifurcation diagram is computed. The resulting codimension-two bifurcation points are identified and included in the three-parameter bifurcation diagram. For simplicity, the continuations of the phenomena associated to the branches NS_1 and NS_2 are described separately below.

5.1. Bifurcations associated to NS_1

The three-parameter bifurcation diagram corresponding to the codimension-two bifurcation points $R^a_{1:1}$, $R^b_{1:1}$, C^a, C^b, and *FNS* appearing in Fig. 5 is depicted in Fig. 16. The continuation of the three Chenciner bifurcations *CH* was not performed. The bifurcation curves are traced from their locations for $\eta_3 = 0.41$ and, for increasing values of η_3, evolve towards the Hopf–Hopf resonant point $HH_{1:2}$ as depicted in Fig. 16(a)–(b). The curve corresponding to *FNS* is not visible in these diagrams since it runs very close to C^b.

A detailed view in the vicinity of $HH_{1:2}$, corresponding to the rectangles in Fig. 16(a)–(b), is shown in Fig. 16(c)–(d). In these figures, the closed curve H_{10} (divided, for convenience, into H^a_{10} and H^b_{10} at the transversality points) corresponds to the failure of the first stability (Lyapunov) index of the Hopf bifurcation H_1. This curve was computed using the frequency domain version of the Hopf bifurcation theorem [28]. On this curve, two distinctive points labeled $H^{a,b}_{20}$ are detected. These points correspond to the vanishing of the second stability index of the Hopf bifurcation H_1 and are the origin of the curves of cusp bifurcations C^a and C^b.

In order to complete the description, a new zoom is performed in the vicinity of $HH_{1:2}$ denoted by the rectangles in Fig. 16(c)–(d)

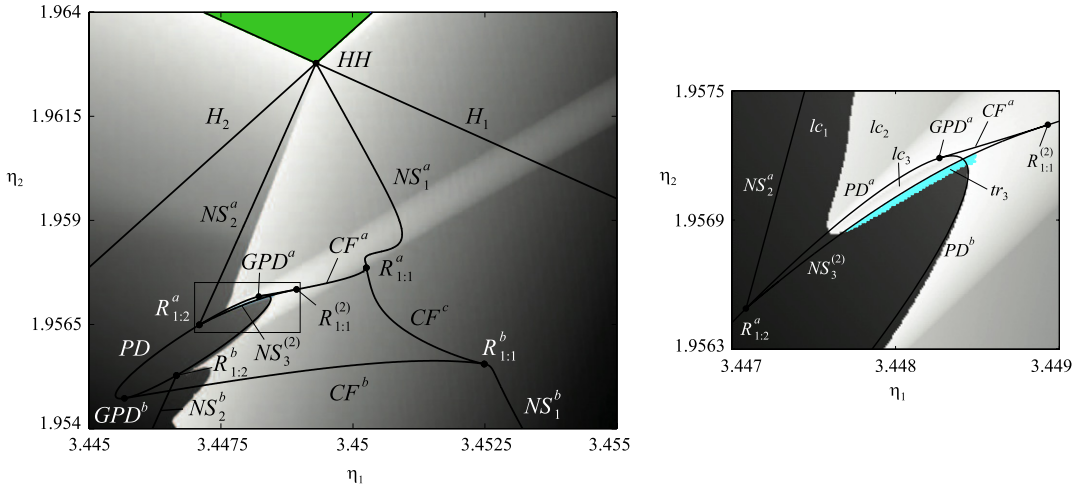

Fig. 15. Lyapunov exponent diagrams. The color coding is as follows. Green: equilibrium point (all the exponents are negative); gray: periodic orbits (one exponent is zero); cyan: 2D torus (two exponents are zero). As the tonality becomes bright, the largest nonzero Lyapunov exponent is closest to zero. (For interpretation of the references to colour in this figure legend, the reader is referred to the web version of this article.)

and shown in Fig. 16(e)–(f). It can be noticed that the curve $R^a_{1:1}$ ends up at the 1:2 Hopf–Hopf resonant point $HH_{1:2}$. The curve is labeled $R^b_{1:1}$ after the transversality failure on the lower right corner. The Fold–Neimark–Sacker (*FNS*) bifurcation curve interacts with the strong resonance $R^b_{1:1}$, leading to a codimension-three singularity (point A in Fig. 16(e)–(f)) with all three nontrivial Floquet multipliers equal to one (see, for example, [29,30] for details on the dynamics associated to this codimension-three bifurcation).

5.2. Bifurcations associated to NS_2

The three-parameter continuation of the main codimension-two bifurcation points associated to the branch NS_2 shown in Fig. 7, i.e. $R^a_{1:2}$, $R^b_{1:2}$, GPD^a and GPD^b, is depicted in Fig. 17. As can be appreciated, these bifurcation curves are organized by the codimension-three singularity $HH_{1:2}$.

In the expanded views of Fig. 17(c)–(d), a transversal intersection of the strong resonance $R^b_{1:2}$ curve and a generalized period-doubling bifurcation GPD^b, denoted by the point B, is detected. As a consequence of this interaction, the resonance $R^b_{1:2}$ changes its structure (a similar phenomena was reported in [27] regarding forced oscillators). In the vicinity, the second stability index of the generalized period-doubling bifurcation GPD^b vanishes at point DPD^b, and a new curve of a cusp bifurcation, namely C^e, arises. The cusp curve (labeled C^c after the transversality failure) evolves towards, and is tangent to, $HH_{1:2}$; therefore it can be concluded that is unfolded by the resonant Hopf–Hopf bifurcation. The associated cuspidal point does not appear in the bifurcation diagram for $\eta_3 = 0.41$ depicted in Fig. 4, since it coalesces near $HH_{1:2}$ due to a swallowtail singularity (*ST*) with C^d for $\eta_3 \simeq 0.414$, as shown schematically in Fig. 18. Then, C^d disappears at the generalized period-doubling bifurcation GPD^a, where a failure of the second stability index of the *PD* bifurcation occurs for $\eta_3 \simeq 0.4147$ (point DPD^a in Fig. 18).

5.3. Bifurcation curves associated to $HH_{1:2}$

The three-parameter scenario in the vicinity of the 1:2 resonant Hopf–Hopf bifurcation point $HH_{1:2}$ is condensed in Fig. 19. The figure shows that this codimension-three singularity unfolds the following bifurcations: a curve of nonresonant Hopf–Hopf bifurcations, a curve of Neimark–Sacker 1:1 strong resonances $R_{1:1}$, a curve of 1:2 resonances $R_{1:2}$, a curve of generalized period-doubling bifurcations *GPD*, a curve of cuspidal points *C*, and a curve H_{10}, where the first stability index of the Hopf bifurcation H_1 fails. Chenciner bifurcation curves are expected to be involved in the unfolding but they were not continued. Therefore, the 1:2 resonant Hopf–Hopf singularity $HH_{1:2}$ unfolds the main bifurcation curves that originate the scenario of Fig. 4. Thus, structures similar to the one depicted in Fig. 4 are expected to be found near $HH_{1:2}$.

6. Further degenerations

As shown in the previous section, the scenario of Fig. 4 is essentially originated by the 1:2 resonant Hopf–Hopf singularity $HH_{1:2}$. Nevertheless, some of the bifurcation curves unfolded by $HH_{1:2}$ exhibit additional nonlinear interactions such as codimension-three bifurcations and transversality failures. The predominant effect is on the cyclic fold bifurcations connecting the structures associated to NS_1 and NS_2. To show this effect schematically, the incidence diagrams of Fig. 20 are included. In Fig. 20, the dashed-line circle separates codimension-one (inside) from codimension-two bifurcations (outside). Bifurcations associated to the branch NS_1 are placed on the right, and on the left appear those corresponding to NS_2. The ensemble of cyclic fold bifurcations connecting the structures associated to NS_1 and NS_2 is denoted by thick lines.

Fig. 20(a) depicts the incidence of bifurcations corresponding to the scenario of Fig. 4 for $\eta_3 = 0.41$. It is clear that cyclic fold curves CF^a and CF^b connect the structures related to NS_1 and NS_2, whereas the bubble denoted by PD^a–PD^b joins $R^a_{1:2}$ with $R^b_{1:2}$, and $CF^{a,b,c}$ join $R^a_{1:1}$ with $R^b_{1:1}$. The scenario remains qualitatively unchanged until the swallowtail (*ST*) bifurcation occurs for $\eta_3 \simeq 0.4140$, where cusps C^c and C^d are created (see Fig. 18). This phenomenon breaks the cyclic fold curve CF^a into three parts $CF^{a,1}$, $CF^{a,2}$, and $CF^{a,3}$, modifying the connection in the upper part of the diagram, as shown in Fig. 20(b). This figure also shows a change in the fold–NS interaction (bottom right), but this phenomenon does not introduce important features, and it is included merely for completeness. For increasing values of η_3, the cusp C^d collapses at the doubly degenerate *PD* singularity DPD^a at $\eta_3 \simeq 0.4147$, and the cyclic fold path in the upper part is simplified (Fig. 20(c)). Finally, near $HH_{1:2}$, the path of the cyclic fold curves between $R^a_{1:1}$ and $R^b_{1:1}$ is broken due to the transversality failure of the curve H_{10}, as depicted in Fig. 20(d). A change in the fold–NS interaction is also shown.

Although the bifurcation scenario near $HH_{1:2}$ is expected to be similar to the one observed in Fig. 4, some of the additional

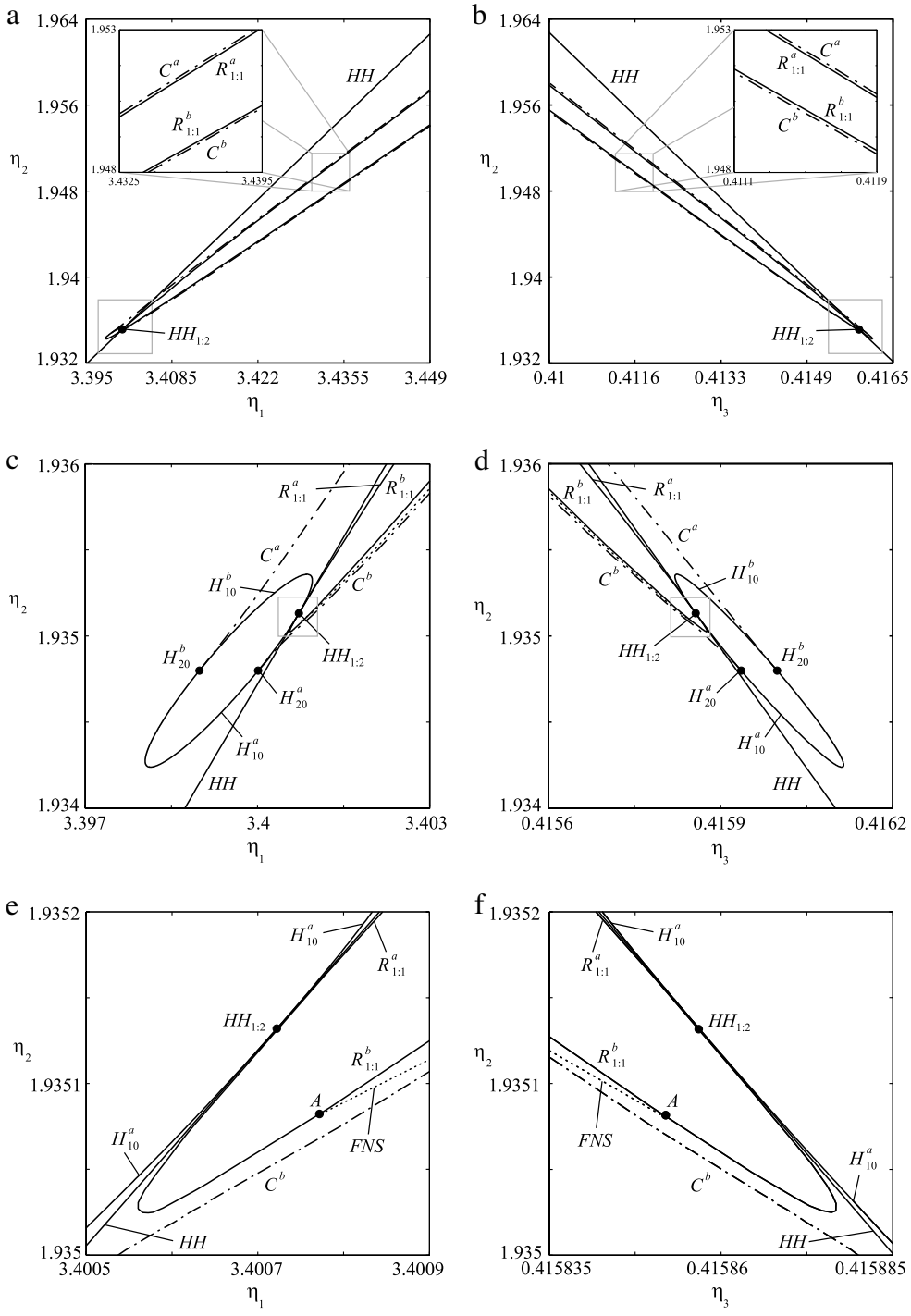

Fig. 16. Three-parameter bifurcation diagram of the codimension-two singularities appearing in the structure associated to NS_1.

phenomena such as the Fold–Neimark–Sacker bifurcation *FNS* and the cusp bifurcations $C^{a,b}$ are introduced by an interaction between the bifurcation curves unfolded by $HH_{1:2}$ and the curve H_{20}. This can be appreciated in the incidence diagram shown in Fig. 21. In this figure, detected codimension-three bifurcations are placed in the first row, followed by codimension-two bifurcations and codimension-one bifurcations in the second and third rows, respectively. Notice that *FNS* and C^b are related to H^a_{20}, that appears on the branch H^a_{10} which is directly connected to $HH_{1:2}$. Therefore, it is conjectured that the whole scenario can be organized in a codimension-four bifurcation occurring when one of the Hopf branches presents a failure of the first and second stability indexes simultaneously with the 1:2 resonant Hopf–Hopf bifurcation.

7. Conclusions

A numerical three-parameter semi-global bifurcation analysis of the 1:2 resonant Hopf–Hopf bifurcation $HH_{1:2}$ has been performed. This codimension-three singularity unfolds a curve of nonresonant Hopf–Hopf bifurcations, curves of Neimark–Sacker 1:1 and 1:2 strong resonances, a curve of generalized period-doubling bifurcations, a curve of cuspidal points, and a curve

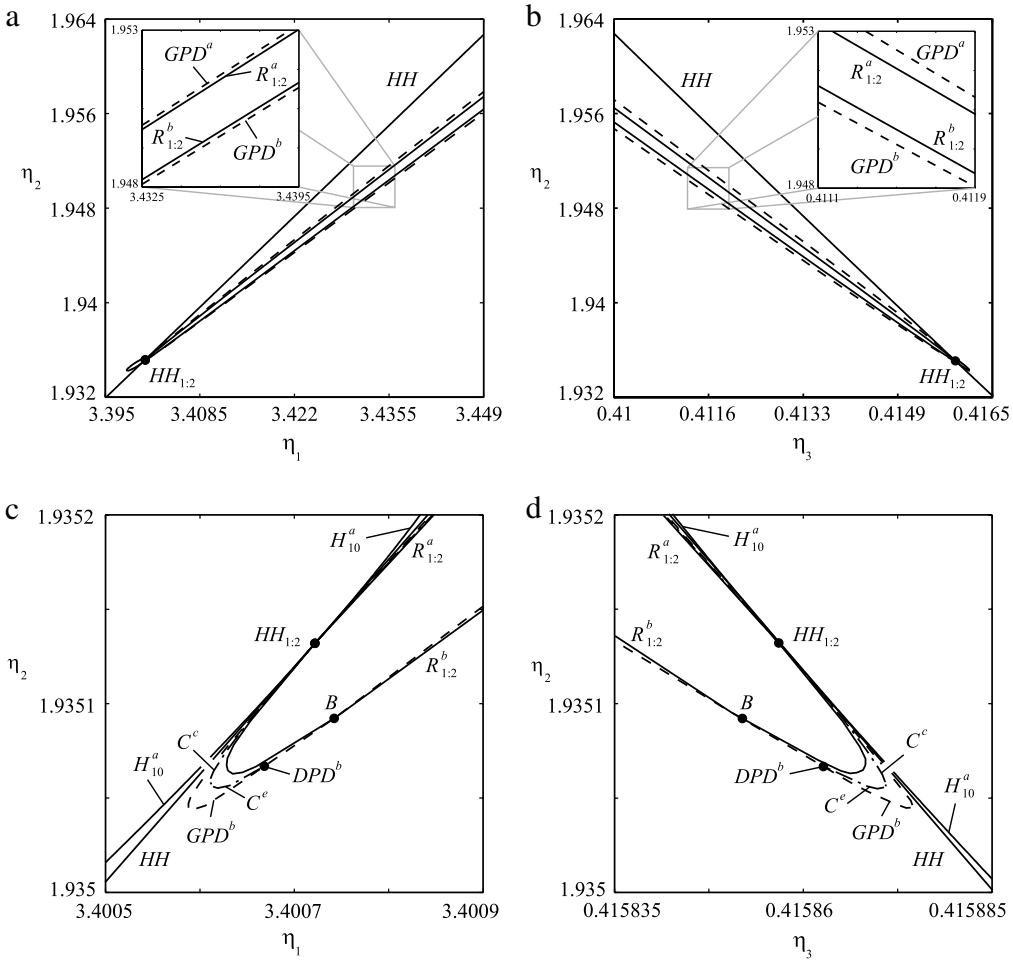

Fig. 17. Bifurcation curves corresponding to the 1:2 strong resonances $R_{1:2}^{a,b}$ and the generalized period-doubling bifurcations $GPD^{a,b}$ of Fig. 7. (a) Projection over (η_1, η_2). (b) Projection over (η_3, η_2).

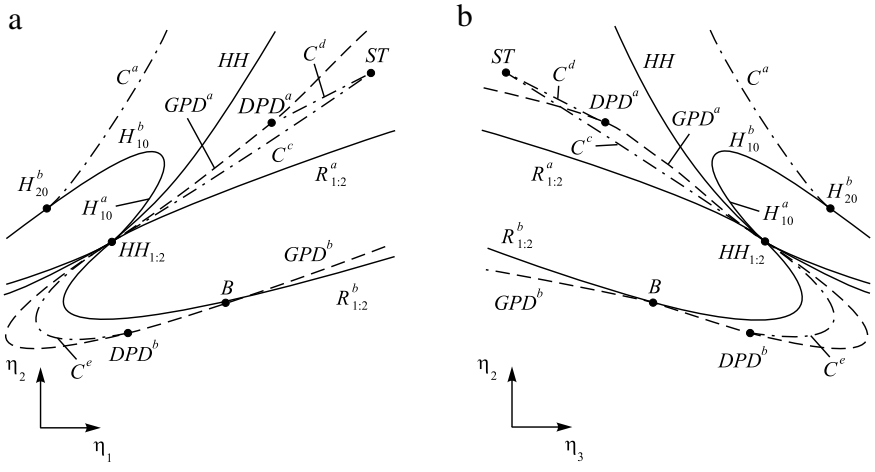

Fig. 18. Schematic view of bifurcation curves $R_{1:2}^{a,b}$, $GPD^{a,b}$ and their interactions near $HH_{1:2}$.

where the first stability index of one of the Hopf bifurcations fails. Chenciner bifurcation curves and global bifurcations are expected to be involved in the unfolding, but they were not continued. The analysis also revealed the presence of several codimension-three singularities in the vicinity of $HH_{1:2}$. One of them corresponds to the simultaneous occurrence of a cyclic fold, a Neimark–Sacker bifurcation, and a 1:1 strong resonance bifurcation, and is characterized by three nontrivial multipliers of the limit cycle equal to one. The others are a swallowtail bifurcation (incidence of two curves of cusps), two doubly degenerate period-doubling bifurcations, and two doubly degenerate Hopf bifurcations. If parameter α_2 is decreased, the bubble H_{10} shrinks and disappears for $\alpha_2 = 0$ (when the quadratic nonlinear term in the circuit model vanishes). This is a codimension-four

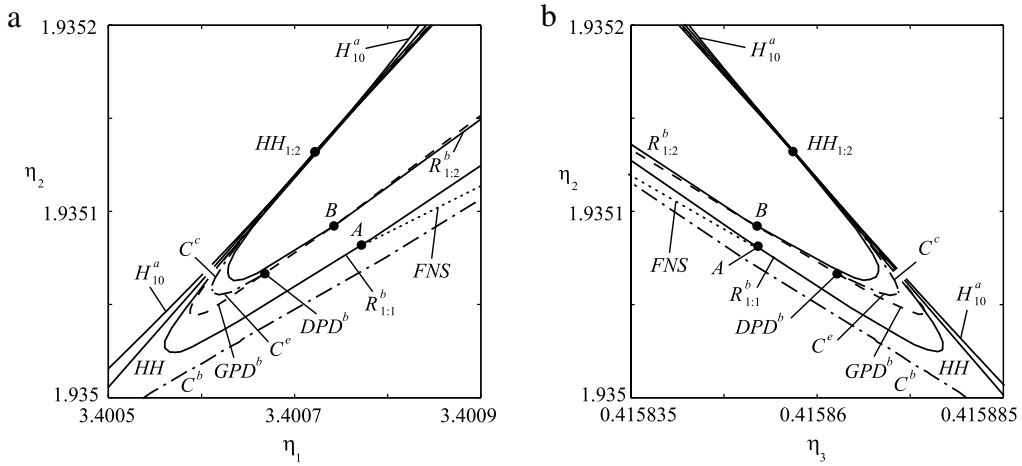

Fig. 19. Three-parameter scenario in the vicinity of the 1:2 resonant Hopf–Hopf bifurcation point HH_{12}.

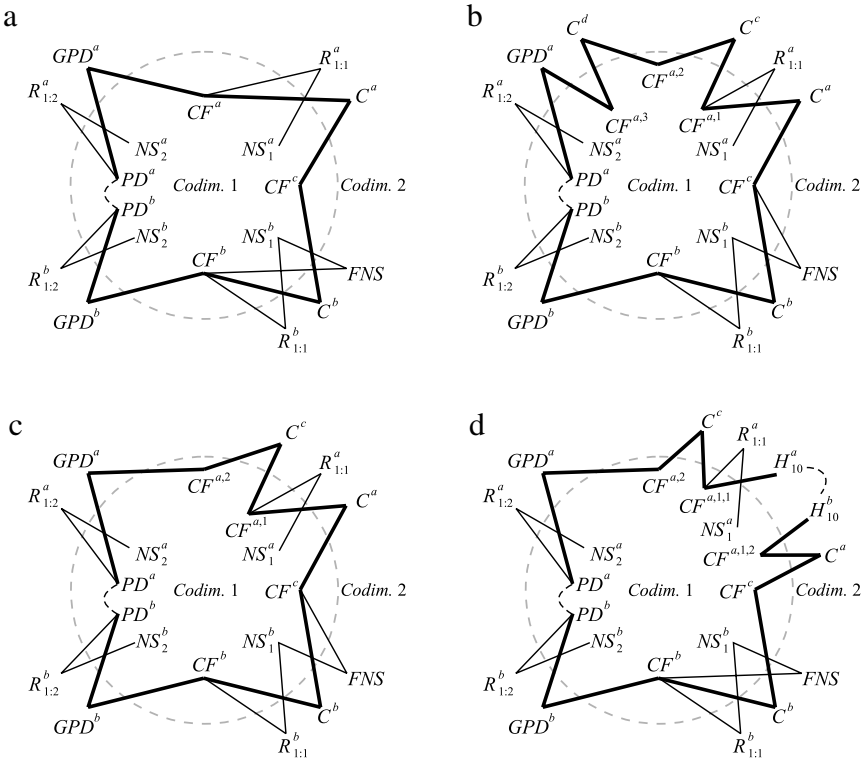

Fig. 20. Incidence diagrams associating the codimension-one (inside the dashed circle) and codimension-two (outside the circle) bifurcations for different values of parameter η_3. (a) Scenario for $\eta_3 \simeq 0.41$ (associated to Fig. 4). (b) Scenario after the swallowtail bifurcation, for $\eta_3 \simeq 0.4140$ (see Fig. 18). (c) After the doubly degenerate period-doubling bifurcation (DPD^a) for $\eta_3 \simeq 0.4147$. (d) Near HH_{12}, after the transversality failure of H_{10} for $\eta_3 \simeq 0.415821$.

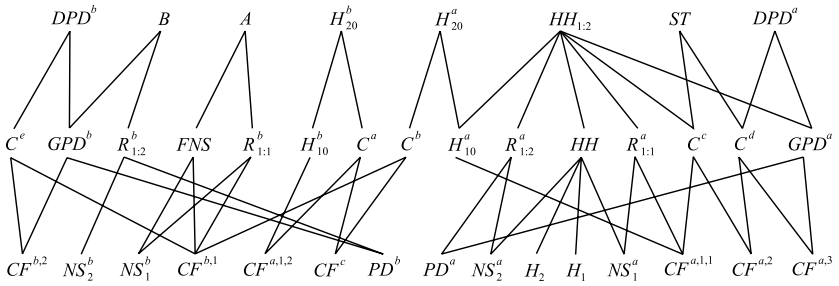

Fig. 21. Incidence diagram connecting codimension-one (bottom row), codimension-two (middle row), and codimension-three (top row) bifurcations.

singularity of the equilibrium point, and it could explain the birth of some of the codimension-three bifurcations near $HH_{1:2}$, but the analysis of this phenomenon is beyond the scope of the paper.

Acknowledgments

The authors appreciate the helpful comments of the three anonymous reviewers on the first version of the manuscript. This work was supported by Universidad Nacional del Sur (PGI 24/K052), Consejo Nacional de Investigaciones Científicas y Técnicas (PIP-112-200801-01112) and Agencia Nacional de Promoción Científica y Tecnológica (PICT-2010-0465).

References

[1] P. Yu, Analysis on double Hopf bifurcation using computer algebra with the aid of multiple scales, Nonlinear Dynam. 27 (2002) 19–53.
[2] P.A. Chamara, B.D. Coller, A study of double flutter, J. Fluids Struct. 19 (2004) 863–879.
[3] J. Xie, W. Ding, Hopf–Hopf bifurcation and invariant torus T^2 of a vibro-impact system, Internat. J. Non-Linear Mech. 40 (2005) 531–543.
[4] G. Revel, D.M. Alonso, J.L. Moiola, A gallery of oscillations in a resonant electric circuit: Hopf–Hopf and fold–flip interactions, Internat. J. Bifur. Chaos 18 (2) (2008) 481–494.
[5] S. Ma, Q. Lu, Z. Feng, Double Hopf bifurcation for van der Pol-Duffing oscillator with parametric delay feedback control, J. Math. Anal. Appl. 338 (2008) 993–1007.
[6] A. Sterk, R. Vitolo, H. Broer, C. Simó, H. Dijkstra, New nonlinear mechanisms of midlatitude atmospheric low-frequency variability, Phys. D 239 (10) (2010) 702–718.
[7] Y.A. Kuznetsov, Elements of Applied Bifurcation Theory, third ed., Springer-Verlag, New York, 2004.
[8] S. Chow, C. Li, D. Wang, Normal Forms and Bifurcation of Planar Vector Fields, Cambridge University Press, Cambridge, 1994.
[9] S.A. Campbell, V.G. LeBlanc, Resonant Hopf–Hopf interactions in delay differential equations, J. Dynam. Differential Equations 10 (2) (1998) 327–346.
[10] J. Xu, K.W. Chung, Double Hopf bifurcation with strong resonances in delayed systems with nonlinearities, Math. Probl. Eng. (2009) Art. ID 759363.
[11] W. Wang, J. Xu, Multiple scales analysis for double Hopf bifurcation with 1:3 resonance, Nonlinear Dynam. 66 (1–2) (2010) 39–51.
[12] A. Luongo, A. Paolone, A. Di Egidio, Multiple timescales analysis for 1:2 and 1:3 resonant Hopf bifurcations, Nonlinear Dynam. 10 (2) (2003) 269–291.
[13] S.A. Van Gils, M. Krupa, W.F. Langford, Hopf bifurcation with non-semisimple 1:1 resonance, Nonlinearity 3 (3) (1990) 825–850.
[14] N. Sri Namachchivaya, M.M. Doyle, W.F. Langford, N.W. Evans, Normal form for generalized Hopf bifurcation with non-semisimple 1:1 resonance, Z. Angew. Math. Phys. 45 (2) (1994) 312–335.
[15] E. Knobloch, M.R.E. Proctor, The double Hopf bifurcation with 2:1 resonance, Proc. R. Soc. Lond. Ser. A 415 (1988) 61–90.
[16] V.G. LeBlanc, W.F. Langford, Classification and unfoldings of 1:2 resonant Hopf bifurcation, Arch. Ration. Mech. Anal. 136 (1996) 305–357.
[17] V.G. LeBlanc, On some secondary bifurcations near resonant Hopf–Hopf interactions, Dynam. Contin. Discrete Impuls. Systems 7 (2000) 405–427.
[18] G. Revel, D.M. Alonso, J.L. Moiola, Interactions between oscillatory modes near a 2:3 resonant Hopf–Hopf bifurcation, Chaos 20 (4) (2010) 0431061–0431068.
[19] F.O.O. Wagener, Semi-local analysis of the k:1 and k:2 resonances in quasi-periodically forced systems, in: H.W. Broer, B. Krauskopf, G. Vegter (Eds.), Global Analysis of Dynamical Systems, Festschrift Dedicated to Floris Takens for his 60th Birthday, Institute of Physics, Bristol, Philadelphia, 2001, pp. 113–129.
[20] H.W. Broer, V. Naudot, R. Roussarie, K. Saleh, F.O.O. Wagener, Organising centres in the semi-global analysis of dynamical systems, Int. J. Appl. Math. Stat. 12 (D07) (2007) 7–36.
[21] H.W. Broer, R. van Dijk, R. Vitolo, Survey of strong normal-internal k:l resonances in quasi-periodically driven oscillators for $l = 1, 2, 3.$, in: G. Gaeta, R. Vitolo, S. Walcher (Eds.), Proceedings of the International Conference on SPT 2007, World Scientific, Otranto, Italy, 2007, pp. 45–55.
[22] G.R. Itovich, J.L. Moiola, Double Hopf bifurcation analysis using frequency domain methods, Nonlinear Dynam. 39 (2005) 235–258.
[23] W. Govaerts, Y.A. Kuznetsov, V. De Witte, A. Dhooge, H.G.E. Meijer, W. Mestrom, A.M. Riet, B. Sautois, MATCONT and CL-MATCONT continuation toolboxes in matlab, Tech. Rep., Gent University and Utrech University, 2011.
[24] K. Saleh, F.O.O. Wagener, Semi-global analysis of periodic and quasi-periodic normal-internal k:1 and k:2 resonances, Nonlinearity 23 (2010) 2219–2252.
[25] H. Broer, C. Simó, R. Vitolo, Hopf saddle–node bifurcation for fixed points of 3D-diffeomorphisms: analysis of a resonance 'bubble', Phys. D 237 (13) (2008) 1773–1799.
[26] R. Vitolo, H. Broer, C. Simó, Routes to chaos in the Hopf-saddle–node bifurcation for fixed points of 3D-diffeomorphisms, Nonlinearity 23 (8) (2010) 1919–1947.
[27] K.B. Hilger, D.S. Luciani, Forced oscillators: a detailed numerical analysis, Master's Thesis, Technical University of Denmark, Lyngby, Denmark, August 1998.
[28] A.I. Mees, L.O. Chua, The Hopf bifurcation theorem and its applications to nonlinear oscillations in circuits and systems, IEEE Trans. Circuits Syst. I 26 (4) (1979) 235–254.
[29] A.L. Shilnikov, L.P. Shilnikov, D.V. Turaev, Normal forms and Lorenz attractors, Internat. J. Bifur. Chaos 3 (5) (1993) 1123–1139.
[30] H.R. Dullin, J.D. Meiss, Quadratic volume-preserving maps: invariant circles and bifurcations, SIAM J. Appl. Dyn. Syst. 8 (2009) 76–128.